

A high-flux entanglement source based on a doubly resonant optical parametric amplifier

Christopher E Kuklewicz, Eser Keskiner, Franco N C Wong and Jeffrey H Shapiro

Research Laboratory of Electronics, Massachusetts Institute of Technology, Cambridge, MA 02139, USA

Received 2 October 2001, in final form 26 November 2001

Published 27 March 2002

Online at stacks.iop.org/JOptB/4/S162

Abstract

A 532 nm pumped type-II phase-matched, doubly resonant KTP optical parametric amplifier (OPA) was operated near frequency degeneracy to yield an inferred downconverted photon pair production rate of $1.7 \times 10^6 \text{ s}^{-1}$ at a pump power of $100 \mu\text{W}$. The OPA output consisted of three components: narrowband doubly resonant mode pairs; narrowband singly resonant mode pairs for which either the signal or idler was resonant with the cavity and broadband nonresonant mode pairs. Under frequency-degenerate operation, the broadband nonresonant mode pairs were polarization triplet states. We observed quantum interference between the orthogonally polarized photons of the triplet states when they were analysed with a polarizer set at 45° relative to the OPA's output polarizations, leading to reduced coincidence counts.

Keywords: Polarization entanglement, optical parametric amplifier, quantum interference, coincidence counting

1. Introduction

The polarization state of a single photon provides a qubit substrate for a variety of quantum information processing applications. Pairs of polarization-entangled photons enable the teleportation of arbitrary quantum states [1] and the implementation of entanglement-based quantum cryptography [2]. Entangled photons are routinely and easily generated by spontaneous parametric downconversion (SPDC) in a nonlinear crystal [3, 4]. Typically, the ultraviolet line of an argon ion laser is used to pump a beta barium borate (BBO) crystal—or two crystals in orthogonal orientations—producing signal and idler outputs with wavelengths near 700 nm. These subharmonics emerge from the crystal in partially overlapping cones, leading to inefficient collection of the downconverted photons. In addition, the bandwidths of these outputs are generally quite large, of the order of several nm in wavelength.

A team of researchers from the Massachusetts Institute of Technology (MIT) and Northwestern University (NU) is developing a singlet-based quantum communication system [5] that uses a novel ultrabright source of polarization-entangled photon pairs [6], and a trapped-atom quantum

memory [7] whose loading can be nondestructively verified and whose structure permits all four Bell-state measurements to be performed. The MIT/NU quantum communication architecture needs a narrowband source (bandwidth ~ 30 MHz) of polarization-entangled photons at 795 nm to match the cavity linewidth and excitation wavelength of its trapped-Rb quantum memories. The standard SPDC approach to producing polarization entanglement is too broadband, and its flux is too low (~ 10 pairs s^{-1} in a 30 MHz bandwidth) to be useful in this regard [4]. Moreover, the SPDC outputs emerge in spatial modes that are ill suited to coupling into the trapped-atom cavity. In this paper, we describe our work on implementing a high-brightness, cavity-enhanced downconversion source and demonstrating the quantum interference behaviour of its outputs.

2. Doubly resonant optical parametric amplifier

Resonating both the signal and idler fields of an optical parametric amplifier (OPA) produces a significant enhancement in the nonlinear interaction, resulting in a variety of salutary effects for quantum communication applications.

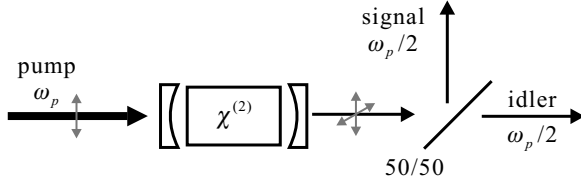


Figure 1. Schematic diagram of a high-flux source of polarization-entangled photon pairs based on a type-II phase-matched degenerate OPA and a 50/50 beamsplitter.

In comparison with the SPDC, the doubly resonant amplifier (DRA) has a substantially lower pump-power threshold for the onset of oscillation and dramatically narrower output bandwidths for its signal and idler. Moreover, the DRA confines these outputs to well defined spatial modes that can be optimally mode matched into trapped-atom cavities. In addition, longer crystals can be utilized to further improve the pair generation efficiency. We have previously proposed a dual-DRA system for generating polarization-entangled singlet states with high brightness [6]. It is also possible, however, to use a simpler single-DRA set-up to generate polarization-entangled triplet states at high brightness, as illustrated in figure 1. In this figure, a type-II phase-matched nonlinear crystal placed inside a linear cavity and pumped at frequency ω_p produces orthogonally polarized signal and idler outputs. Consider the doubly resonant modes at exact frequency degeneracy—signal and idler outputs exactly at frequency $\omega_p/2$ —that propagate collinearly in the same spatial mode. The state of a photon pair in these output modes is

$$|\Psi\rangle = |1\rangle_{\uparrow}|1\rangle_{\bullet}, \quad (1)$$

where \uparrow and \bullet refer to vertical and horizontal polarizations, respectively. Each photon in this pair has a 50/50 chance of appearing in either output port of the beamsplitter shown in figure 1. When one photon appears in each output port—something that can be post-selected by placing single-photon detectors in these output ports and monitoring for coincidences—the joint state of the beamsplitter’s outputs is the polarization-entangled triplet,

$$|\Psi\rangle_{\text{BS}} = (|1\rangle_{\text{S}\uparrow}|1\rangle_{\text{I}\bullet} + |0\rangle_{\text{S}\bullet}|0\rangle_{\text{I}\uparrow} + |0\rangle_{\text{S}\uparrow}|0\rangle_{\text{I}\bullet} + |1\rangle_{\text{S}\bullet}|1\rangle_{\text{I}\uparrow})/\sqrt{2}, \quad (2)$$

because of indistinguishability. This simple argument shows that the degenerate DRA system can be utilized to generate a polarization-entangled triplet at the expense of a 50% loss. A more elaborate analysis [8] demonstrates that this degenerate DRA source can be used in the MIT/NU quantum communication architecture in lieu of the more efficient, but more complicated, dual-DRA entanglement source.

As confirmed in our experiment (described below), the signal and idler outputs from a DRA are composed of three components. When tuned appropriately, there will be one narrowband doubly resonant mode pair from the DRA [9]. In addition, however, there are narrowband singly resonant mode pairs, for which either the signal or idler field is resonant with the cavity. There are also broadband nonresonant mode pairs, for which neither of the output fields is resonant with the cavity. We can quantify the respective contributions of these three components to the full output flux of the DRA as follows.

The generation rate for the doubly resonant mode pair is given by [6]

$$R_2 = G^2\Gamma, \quad (3)$$

where G^2 is the pump power level normalized to the pump threshold power, typically of the order of 0.01 for quantum communication applications, and Γ/π is the cavity bandwidth, of the order of tens of MHz.

Interpretation of equation (3) requires a clear understanding—both theoretically and experimentally—of what constitutes a photon pair in an OPA set-up. The doubly resonant signal and idler modes have bandwidths of the order of Γ/π . Thus a signal and idler photon pair that are created in near simultaneity within the nonlinear crystal may emerge from the cavity with timing jitters on the order of $1/\Gamma$. We define a pair—both theoretically and experimentally—by counting signal/idler coincidences that occur within a time window T_c satisfying $\Gamma T_c \gg 1$. Note that this is not the $T_c \rightarrow \infty$ limit, because we must also require $G^2\Gamma T_c \ll 1$, for the doubly resonant signal and idler pairs, to ensure that with high probability at most one pair is present in any T_c -duration interval. Because there will also be singly resonant and nonresonant modes emitted by the DRA, the upper limit on the coincidence interval is actually set by the condition $(R_0 + R_1 + R_2)T_c \ll 1$, where the singly resonant pair-generation rate, R_1 , and the nonresonant pair-generation rate, R_0 , are given below. Inasmuch as all three generation rates are proportional to G^2 , it is always possible to simultaneously satisfy $\Gamma T_c \gg 1$ and $(R_0 + R_1 + R_2)T_c \ll 1$ by operating the DRA at low enough gain.

The singly resonant pair production rate can be found from the doubly resonant rate via

$$R_1 = 2R_2 \left(\frac{(T+L)^2}{4T} \right) \left(\frac{B_{\text{SRO}}}{B_{\text{DRO}}} \right) \left(\frac{B_{\text{PM}}}{\text{FSR}} \right), \quad (4)$$

where T is the output coupler transmission, L is the cavity’s roundtrip excess loss, $B_{\text{SRO}} = \Gamma/\pi$ is the bandwidth of a singly resonant oscillator (SRO) cavity, $B_{\text{DRO}} = (\sqrt{2} - 1)^{1/2} B_{\text{SRO}}$ is the bandwidth of a doubly resonant oscillator (DRO) cavity, B_{PM} is the phase-matching bandwidth of the crystal and FSR is the average free spectral range of the cavity. The effective threshold power in singly resonant pair generation is raised, because the enhancement due to the second resonance is no longer available. This decreased pumping level leads to the first factor in parentheses on the right in equation (4) [10]. The second term in parentheses is the ratio of the effective cavity bandwidths for the singly resonant and doubly resonant modes. Typically, by design, there is only one doubly resonant mode pair in type-II phase matching [9], but singly resonant mode pairs occur every free spectral range FSR. This leads to the final factor in parentheses, which accounts for the number of such mode spacings that occur within the crystal’s phase-matching bandwidth B_{PM} . The factor of two on the right in equation (4) arises from there being two sets of singly resonant modes pairs, one when the signal is resonant and one when the idler is resonant.

The flux of the broadband nonresonant mode pairs also satisfies a simple scaling relation with respect to the doubly resonant flux:

$$R_0 = R_2 \left(\frac{(T+L)^2}{4T} \right)^2 \left(\frac{B_{\text{PM}}}{B_{\text{DRO}}} \right). \quad (5)$$

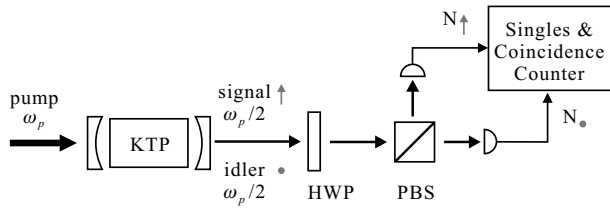


Figure 2. Schematic diagram of experimental set-up for photon counting measurements of the outputs from a frequency-degenerate KTP DRA. HWP = half-wave plate; PBS = polarizing beamsplitter.

Here, the cavity-enhancement factor is squared because there is no resonance for either field, and the bandwidth factor represents the output's coming from the entire phase-matching bandwidth rather than just the doubly resonant bandwidth. For our DRA system, we have $T = 2.7\%$, $L = 0.56\%$, $B_{\text{SRO}} = 30$ MHz, $B_{\text{DRO}} = 20$ MHz, $B_{\text{PM}} = 320$ GHz and $\text{FSR} = 5.6$ GHz. Thus, we expect that our DRA system will have 36% of its output flux coming from nonresonant mode pairs, 41% coming from singly resonant mode pairs and the remaining 23% coming from doubly resonant mode pairs.

3. Experimental set-up

Figure 2 shows a schematic diagram of our experimental set-up. We used a 10 mm long hydrothermally grown potassium titanyl phosphate (KTP) crystal as the nonlinear optical medium, which we pumped at 532 nm with a continuous-wave, frequency-doubled Nd:YVO₄ laser to obtain signal and idler outputs at 1064 nm. This KTP DRA system had previously been used to generate ~ 5.5 dB of sub-shot-noise intensity correlation in above-threshold, i.e. optical parametric oscillator, operation [11]. It is a well characterized system that possesses many desirable operating advantages, for example a large nonlinear coefficient, a high escape efficiency of $\sim 83\%$ and noncritical phase matching with very little Poynting-vector walkoff ($\sim 0.23^\circ$) among the interacting beams within the KTP crystal. However, this DRA's 1064 nm output wavelength is not at the 795 nm wavelength needed for the Rb-atom quantum memory, and a Si single-photon detector has a quantum efficiency of $\sim 1\text{--}2\%$ at this output wavelength. Despite this severe detection-efficiency disadvantage, we shall show that the KTP DRA provided a clear initial experiment for demonstrating and characterizing cavity-enhanced downconversion.

The cavity consisted of a 20 cm radius-of-curvature input mirror that was coated for maximum reflection at 1064 nm and maximum transmission at 532 nm, together with a 2 cm radius-of-curvature output mirror that was coated for 2.7% transmission at 1064 nm and maximum reflection at 532 nm. Hence the linear cavity was designed to resonate the subharmonic signal and idler fields at 1064 nm in a double-pass pump configuration. The $3 \times 3 \times 10$ mm hydrothermally grown KTP crystal was antireflection coated at both the pump and the output wavelengths to minimize intracavity losses. The average roundtrip power loss for the vertical and horizontal polarizations was $L = 0.56\%$ and the output coupling was measured to be $T = 2.7\%$, so that the escape ratio $T/(T + L)$ is $\sim 83\%$. The oscillation threshold for the KTP system was ~ 350 mW of pump power [11].

The two cavity mirrors were physically separated by 1.9 cm, corresponding to a cavity free spectral range $\text{FSR} = 5.6$ GHz. To permit cavity-length scanning, the input mirror was mounted on a piezoelectric transducer (PZT), which was rigidly attached to a mounting cage. The output mirror was also rigidly attached to the mounting cage for best stability. The crystal was mounted on a thermo-electric (TE) cooler for fine temperature tuning, and the TE cooler was in turn attached to a rotation stage for changing the crystal's phase-matching angle. The three tuning elements (crystal angle, TE cooler and PZT) permitted the KTP's phase matching to be tuned close to frequency degeneracy at the 532 nm pump wavelength.

In order to eliminate the 1064 nm leakage light ($< 1 \mu\text{W}$) from the pump laser, three short-pass filters (each with transmission of 96% at 532 nm and 0.001% at 1064 nm) were used to filter the pump prior to its entering the DRA cavity. Further discrimination against this leakage light was achieved by the input mirror's having a 1064 nm transmission coefficient of less than $\sim 0.01\%$. Together, these measures ensured that there was no external injection of 1064 nm light into the cavity. At the output of the DRA cavity, a long-pass filter was used to attenuate the residual pump beam without affecting the 1064 nm outputs. The collinearly propagating signal and idler outputs were collimated and then passed through a half-wave plate (HWP) followed by a polarizing beamsplitter (PBS). The HWP allowed a rotation of the outputs that could be analysed by the PBS. The use of a dispersing prism and irises in each output path of the PBS precluded pump light from entering the Perkin Elmer model SPCM-AQR-14 single-photon detectors (SPDs), which were well shielded from stray light. The SPDs had dark count rates of $< 100 \text{ s}^{-1}$. Their quantum efficiencies—estimated from measurements with a calibrated and attenuated laser source—were $\sim 1.5\%$ at 1064 nm. When the cavity escape ratio and propagation losses were included, the overall detection efficiency was estimated to be $\sim 1\%$.

Singles counts from either detector were usually measured by sending the output from the SPD to a computer-based counter and displaying the results on the computer in real time. For coincidence counts, the outputs from the two SPDs were recorded as two time traces using a two-channel computer-based digital oscilloscope that could store 2 million data points per channel. Typically, we used 10 ns sampling intervals (the minimum is 2 ns), and collected 20 ms of samples before transferring the oscilloscope data to the computer for storage and subsequent processing. Multiple 20 ms long data sequences were used for the coincidence-count analysis. This data acquisition procedure afforded us considerable postdetection flexibility in examining and analysing the output pulse sequences. As detailed in the next section, we used this flexibility to study the dependence of the number of coincidences on the duration of the coincidence interval.

4. Experimental results

Figure 3 shows a measurement of the singles counts versus cavity length as we scanned the PZT. These data were taken with 3 mW of pump power, with each data point representing 10 ms of SPD counts. The periodic behaviour in figure 3 occurring with a 266 nm peak-to-peak spacing is due to there

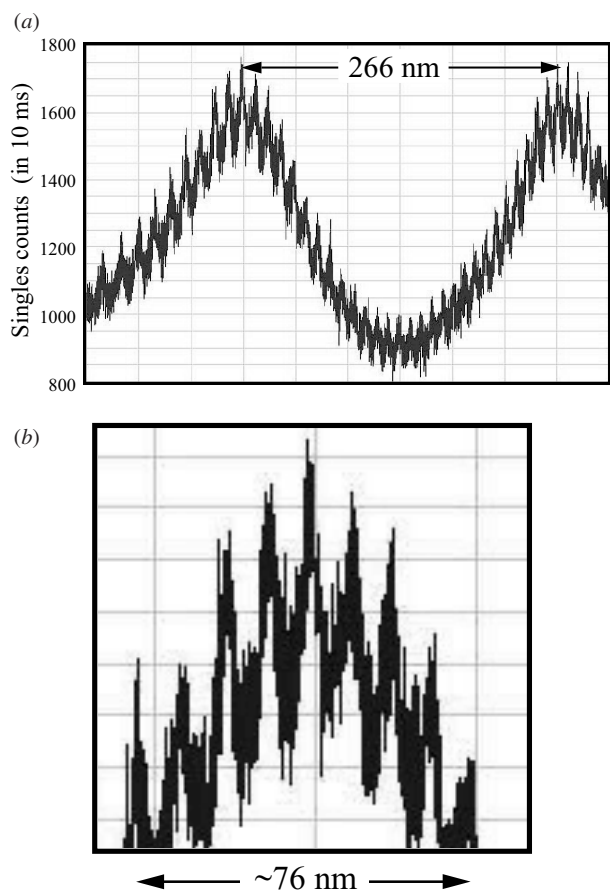


Figure 3. (a) Singles counts of KTP DRA as a function of cavity length tuning; (b) an expanded view of (a) to show the double-resonance modulation peaks. The DRA was pumped at 3 mW and the counting time bin was 10 ms. Weak cavity resonance of the 532 nm pump yields the peak-to-peak cavity length change of 266 nm.

being a very weak residual cavity resonance at the 532 nm pump wavelength. The smaller, higher-spatial-frequency modulation of the singles shown in figure 3(a) is due to the sequence of double resonances that were encountered as the cavity was scanned. Figure 3(b) shows an expanded section of the double-resonance peaks, indicating that they appear regularly at a 9.5 nm cavity-length spacing, a value which agrees with the expected spacing of doubly resonant peaks for an above-threshold DRO [9]. It follows that the baseline counts in figure 3(a)—the minima between the double-resonance peaks—represent the detected singles from the nonresonant mode pairs (R_0) plus the singly resonant mode pairs (R_1). The ratio of the doubly resonant counts to the total counts is $\sim 15\%$, a number that is close to our $R_2/(R_0 + R_1 + R_2) \sim 23\%$ estimate, given our uncertainties in estimating the various bandwidths and the sensitivity of R_2 to cavity alignment. We estimate from figure 3 a peak detection rate of $170\,000\text{ s}^{-1}$ for a 3 mW pump. Assuming an overall detection efficiency of 1%, this corresponds to a signal (idler) production rate of $1.7 \times 10^7\text{ photons s}^{-1}$.

For coincidence measurements, the cavity was free running, with estimated cavity-length fluctuations of no more than a few nm over a 60 s time duration. The DRA output polarizations were rotated with the HWP by either

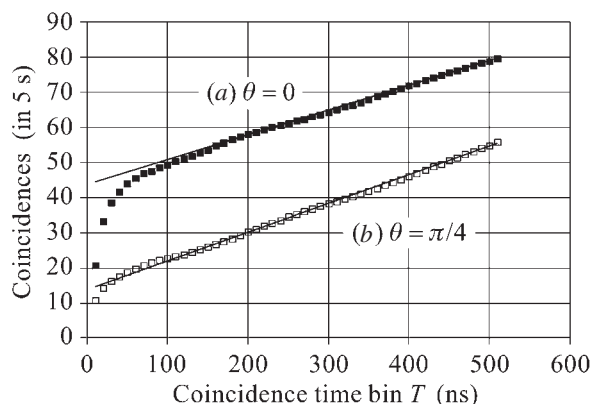


Figure 4. Coincidence counts versus time bin T for $T_M = 5\text{ s}$: (a) $\theta = 0$, and (b) $\theta = \pi/4$. Straight-line fits of the $T > 150\text{ ns}$ data yield coincidence intercepts of 44 for (a) and 14 for (b).

$\theta = 0$ or $\pi/4$. At $\theta = 0$, the orthogonally polarized signal and idler photons of all three output components were separated by the PBS and perfect coincidences should occur for unity quantum efficiency detection. In postdetection processing we took a $T_M = 5\text{ s}$ measurement interval and, within that interval, computed $C(T)$, the average number of coincidences that occurred in a duration- T time bin. The data were taken with a pump power of $\sim 100\ \mu\text{W}$ and the average singles counts for $\theta = 0$ were 20 000 over the 5 s measurement interval. For data taken with $\theta = \pi/4$, the average singles counts were slightly higher, 22 000, over the same 5 s measurement interval. The solid squares in figure 4 show $C(T)$ versus T with no rotation of the output polarization ($\theta = 0$). The 5 s measurement interval required 250 sets of 20 ms long outputs from our digital oscilloscope. For small values of T , figure 4 shows that $C(T)$ for $\theta = 0$ decreases sharply. This fall-off is because the average photon lifetime in the DRA cavity was of the order of 10 ns; the coincidence interval must be appreciably longer than the intracavity photon lifetime to have high confidence that both the signal and the idler photons have been emitted [6]. Beyond the short- T region, the $\theta = 0$ data points for $T > 150\text{ ns}$ in figure 4 can be fitted to a straight line whose $T = 0$ intercept is $C_{\text{int}}(0) = 44$. As we shall explain below, this intercept gives the true value of the coincidence counts, namely, the value that prevails when T is much greater than the DRAs intracavity photon lifetime and accidental coincidences are eliminated. Note that the singles rate and the coincidence interval employed here satisfy the pair definition criteria discussed in the previous section.

The open squares in figure 4 show $C(T)$ versus T obtained from $T_M = 5\text{ s}$ data taken with $\theta = \pi/4$. We see that the slopes of the two $C(T)$ curves in figure 4 are essentially the same, but their $T = 0$ intercepts are different: $C_{\text{int}}(0) = 14$ for $\theta = \pi/4$, whereas $C_{\text{int}}(0) = 44$ for $\theta = 0$. Part of this reduction was due to a 50/50 beamsplitter effect for frequency distinguishable photons with the rest being a consequence of quantum interference between the broadband nonresonant photons, as we shall explain in the next section.

5. Analysis

First consider the $\theta = 0$ case, in which the signal and idler polarizations are aligned with the PBS analyser. From [6, 12]

we have that the signal and idler from the continuous-wave DRA are in a zero-mean joint Gaussian state that is completely characterized by the following normally ordered and phase-sensitive correlation functions:

$$K^{(n)}(\tau) = \langle \hat{E}_s^\dagger(t+\tau) \hat{E}_s(t) \rangle e^{-i\omega_s \tau} = \langle \hat{E}_i^\dagger(t-\tau) \hat{E}_i(t) \rangle e^{i\omega_i \tau}, \quad (6)$$

and

$$K^{(p)}(\tau) = \langle \hat{E}_s(t+\tau) \hat{E}_i(t) \rangle e^{i[(\omega_s+\omega_i)t+\omega_s\tau]}, \quad (7)$$

where $\{\hat{E}_k(t), \omega_k\}$, for $k = s, i$, are the photon-units, positive-frequency field operators of the signal and idler and their respective centre frequencies. Explicit expressions for these correlation functions when only the doubly resonant mode pairs are present are given in [6]; their magnitudes peak at zero delay, $\tau = 0$, and for low gain values ($G^2 \ll 1$) their delay-widths are approximately equal to the intracavity photon lifetime.

The average number of T -time-bin singles counts collected in a measurement interval T_M , when $\theta = 0$, is identical for the two detectors and given by

$$S(T) = (T_M/T) \langle \hat{N}_\uparrow \rangle = (T_M/T) \langle \hat{N}_\bullet \rangle = \eta T_M K^{(n)}(0), \quad (8)$$

where η is the overall detection efficiency, and $\{\hat{N}_\uparrow, \hat{N}_\bullet\}$ are the number operators for T -time-bin photon counting on the vertically and horizontally polarized outputs from the PBS. This theoretical result for the singles counts is easily understood. From its definition we see that $\eta K^{(n)}(0) = \eta \langle \hat{E}_k^\dagger(t) \hat{E}_k(t) \rangle$, for $k = s, i$, is the average number of detected photons per unit time from either DRA output. Because orthogonally polarized signal and idler photons are produced in pairs, their singles counts should be identical and given by the average number of detected photons in a T time bin multiplied by the number of these time bins in the T_M measurement time interval. Note that we have neglected dark counts in this singles analysis—and we shall continue to do so in the coincidence analysis to come—because our experimental singles rate of 4000 s^{-1} greatly exceeds the 100 s^{-1} dark-count rate of our SPDs. Also note that we have assumed equal overall detection efficiencies for the signal and idler, which is very reasonable given that we are operating at frequency degeneracy with identical SPDs.

The average number of T -time-bin coincidences that occur within a T_M measurement interval, $C(T)$, can be derived from the analysis in [12]. The result that is obtained is¹

$$C(T) = (T_M/T) \langle \hat{N}_\uparrow \hat{N}_\bullet \rangle \quad (9)$$

$$= T T_M [\eta K^{(n)}(0)]^2 + \eta^2 T_M \int_{-T}^T d\tau \left(1 - \frac{|\tau|}{T}\right) |K^{(p)}(\tau)|^2 \quad (10)$$

$$\approx T T_M [\eta K^{(n)}(0)]^2 + \eta^2 T_M \int_{-\infty}^{\infty} d\tau |K^{(p)}(\tau)|^2, \quad (11)$$

¹ Strictly speaking, equation (9) overcounts coincidences, because the product of the \hat{N}_\uparrow and \hat{N}_\bullet measurements on a single duration- T bin can exceed unity. We have performed a more complicated analysis to derive $C(T) \equiv \langle u(\hat{N}_\uparrow \hat{N}_\bullet) \rangle$, where $u(\cdot)$ is the unit-step function. This definition of $C(T)$ does not lead to overcounting of coincidences. In the regime of interest here—when T greatly exceeds the cavity lifetime, the DRA is operated at low gain ($G^2 \ll 1$), and the overall detection efficiency is low ($\eta \ll 1$)—the more complicated analysis yields equation (11) for $\theta = 0$, and equation (14) for $\theta = \pi/4$.

where the approximation is valid when T greatly exceeds the DRA's intracavity photon lifetime. In agreement with our coincidence measurements, theory predicts a straight-line relationship between $C(T)$ and T in the long- T limit. The first term in equation (11) is linearly proportional to T and equal to the number of accidental coincidences for two independent Poisson processes. The second term in this expression, which has no T dependence, is the theoretical prediction for $C_{\text{int}}(0)$, the coincidence intercept at $T = 0$. The entanglement between the signal and idler beams is intimately connected to the phase-sensitive correlation function that appears in $C_{\text{int}}(0)$ [12]. When $K^{(p)}(\tau) = 0$ for all τ , the joint signal and idler state becomes a multi-mode Gaussian mixture of coherent states, and the coincidence counts reduce to accidental Poisson occurrences. On the other hand, when the DRA has no excess loss and is operated at low gain ($G^2 \ll 1$), the integral appearing in $C_{\text{int}}(0)$ equals $K^{(n)}(0)$. In this regime, we have perfect signal/idler pair creation: $C_{\text{int}}(0) = \eta^2 T_M K^{(n)}(0)$, namely, the average number of T -time-bin coincidences in the T_M measurement interval equals the DRA's signal (or idler) flux $K^{(n)}(0)$ multiplied by the measurement interval and reduced by an efficiency factor η for each of the two detectors employed in the coincidence measurement.

Equation (11) shows that $\eta = C_{\text{int}}(0)/S(T)$ when the DRA has no excess loss. Our $\theta = 0$ data— $C_{\text{int}}(0) = 44$ and $S(T) = 2 \times 10^4$ —thus yield the effective detection quantum efficiency of our experiment, $\eta = 0.22\%$. Equation (11) also shows that the ratio of the coincidence slope to $S(T)$ equals $S(T)/T_M$. Using the $\theta = 0$ coincidence slope from figure 4 and our measured value of $S(T)$ then implies an $S(T)/T_M$ value of 3500, which is in reasonable agreement with the directly measured $S(T)/T_M$ value of 4000. Taking the average of these two rates, we estimate that the pair production rate of our DRA system (for $\eta = 0.22\%$) was $\sim 1.7 \times 10^6 \text{ s}^{-1}$ for this set of data. From our $\sim 1.5\%$ laser-based estimate of the SPD's intrinsic quantum efficiency, the $\sim 83\%$ cavity escape efficiency, and our $\sim 20\%$ propagation and coating losses, we should have had $\sim 1\%$ overall detection efficiency. The coincidence-inferred $\eta = 0.22\%$ value therefore indicates the presence of additional losses. Prime possibilities include an overestimate of the escape efficiency for the nonresonant mode pairs, spatial misalignment and an overestimate of the detectors' intrinsic quantum efficiency. The inferred generation rate over the phase-matching bandwidth $B_{\text{PM}} = 320 \text{ GHz}$ is $\sim 5.3 \times 10^4 \text{ pairs s}^{-1} \text{ GHz}^{-1} \text{ mW}^{-1}$, in units of pairs per second per GHz of bandwidth per mW of pump power. In comparison, the broadband source of Kwiat *et al* [4] yields $1.5 \times 10^6 \text{ s}^{-1}$ over a 3 THz bandwidth with 150 mW of pump, or 3 pairs $\text{s}^{-1} \text{ GHz}^{-1} \text{ mW}^{-1}$.

The preceding analysis and comparison with experiment applies to the $\theta = 0$ case, and is independent of how close to frequency degeneracy we were able to tune the DRA. In order to generate the triplet state by beam splitting the output from a DRA, however, we do need to operate at frequency degeneracy. The bandwidths of the singly resonant and doubly resonant mode pairs are so small, in our experiment, that we do not expect them to be frequency degenerate as we made no special effort to realize such a difficult-to-achieve degeneracy. On the other hand, the 320 GHz bandwidth of the nonresonant mode pairs was large enough that we did tune this component

to frequency degeneracy in our experiments. Consequently, a nonresonant photon pair whose individual photons appear at frequencies $\omega_{\pm} \equiv \omega_p/2 \pm \Delta\omega$ was in the triplet state,

$$|\Psi\rangle_{\text{SI}} \equiv (|\uparrow\rangle_{\omega_+}|\bullet\rangle_{\omega_-} + |\bullet\rangle_{\omega_+}|\uparrow\rangle_{\omega_-})/\sqrt{2}. \quad (12)$$

A polarization rotation of $\pi/4$ converts $|\Psi\rangle_{\text{SI}}$ into another triplet,

$$|\Psi'\rangle_{\text{SI}} \equiv (|\uparrow\rangle_{\omega_+}|\uparrow\rangle_{\omega_-} + |\bullet\rangle_{\omega_+}|\bullet\rangle_{\omega_-})/\sqrt{2}. \quad (13)$$

When $|\Psi'\rangle_{\text{SI}}$ encounters the PBS, its two photons always take the same output path. Thus, although which path they take occurs with equal probability, the fact that they both go the same way precludes the occurrence of coincidence counts on the PBS outputs. A more rigorous treatment of this quantum interference effect—based on the Gaussian-state coincidence analysis from [12]—gives the following low-flux, long- T -limit expression for the average number of T -time-bin coincidences in the T_M measurement interval when $\theta = \pi/4$:

$$C(T) = (T_M/T)\langle\hat{N}_\uparrow\hat{N}_\bullet\rangle \approx TT_M[\eta K^{(n)}(0)]^2 + \eta^2 \frac{T_M}{2} \int_{-\infty}^{\infty} d\tau \{ |K^{(p)}(\tau)|^2 - \text{Re}[K^{(p)}(\tau)K^{(p)*}(-\tau)e^{-i(\omega_s - \omega_i)\tau}] \}. \quad (14)$$

Once again we find that there is a straight-line relationship between $C(T)$ and T . The first term on the right in equation (14), which is linearly proportional to T , is again the number of accidental coincidences for two independent Poisson processes, as seen previously in equation (11). Thus, theory predicts identical coincidence slopes for the $\theta = 0$ and $\pi/4$ data, behaviour that is confirmed by the experimental curves in figure 4. The constant term on the right in equation (14) is the coincidence intercept $C_{\text{int}}(0)$. That equation (14) contains a $C_{\text{int}}(0)$ factor of $T_M/2$ whereas equation (11) has a factor of T_M in this term is simply a beamsplitter effect. After the $\pi/4$ polarization rotation, the PBS acts as a 50/50 beamsplitter for frequency-nondegenerate and hence distinguishable signal/idler photon pairs. For such pairs, there is a 50/50 chance that both will exit the same output port from the PBS. So, whatever coincidence rate these pairs would otherwise have produced is reduced by a factor of two. The second term within the integrand of equation (14) is due to quantum interference. For nondegenerate DRA operation—when $|\omega_s - \omega_i|$, the centre-frequency difference between the signal and idler fluorescence spectra, greatly exceeds the inverse of the delay-width of the phase-sensitive correlation function $K^{(p)}(\tau)$ —this quantum interference term integrates to zero, and we are left with a $\theta = \pi/4$ coincidence intercept equal to half of its $\theta = 0$ value. That is, were there no quantum interference in our experiment, $C_{\text{int}}(0)$ for $\theta = \pi/4$ in figure 4 should have been ~ 22 .

For the frequency-degenerate operation, i.e. $\omega_s = \omega_i$, and a symmetric phase-sensitive correlation function, $K^{(p)}(\tau) = K^{(p)}(-\tau)$, we obtain perfect quantum interference. The second term in equation (14) then equals zero and $C(T)$ reduces to the result for accidental Poisson coincidences, for which $C_{\text{int}}(0) = 0$ prevails. So, had there only been broadband nonresonant mode pairs present in our experiment, then the output after the HWP— $|\Psi'\rangle_{\text{SI}}$ from equation (13)—would not give any coincidences.

The $\theta = \pi/4$ data in figure 4 show the presence of quantum interference arising from the frequency-degenerate, broadband nonresonant mode pairs. Our measured value of the intercept ratio,

$$r_{\text{int}} \equiv \frac{C_{\text{int}}(0)|_{\theta=\pi/4}}{C_{\text{int}}(0)|_{\theta=0}} = \frac{14}{44} = 0.32, \quad (15)$$

confirms this assertion. Suppose that the nonresonant mode pairs gave perfect quantum interference and that the singly resonant and doubly resonant pairs gave none. Then, the intercept ratio should obey

$$r_{\text{int}} = \frac{(R_1 + R_2)/2}{R_0 + R_1 + R_2}. \quad (16)$$

We have already estimated the relative contributions of the nonresonant, singly resonant and doubly resonant mode pairs to be 36, 41 and 23%, respectively, yielding $r_{\text{int}} = 0.32$, in excellent agreement with the observed value. However, a more realistic scenario is that the DRA cavity was not tuned to the peak of double resonance, in which case $R_2 = 0$ and $r_{\text{int}} = 0.27$, which implies that we should have fewer coincidences than we observed. Perhaps the most likely case is that we have some doubly resonant mode pairs and that the quantum interference for the nonresonant mode pairs was imperfect, such as might have been caused by imperfect spatial mode matching or by Poynting-vector walkoff between the signal and idler beams.

6. Conclusion

In summary, we have demonstrated a high-flux entanglement source based on a doubly resonant OPA. We have shown that the output is composed of three distinct components: broadband nonresonant mode pairs, narrowband singly resonant mode pairs and narrowband doubly resonant mode pairs. When the DRA system was operated at frequency degeneracy, we observed quantum interference from the broadband nonresonant mode pairs, suggesting that these broadband photon pairs were polarization-entangled triplets. From estimates of the intrinsic production rate (i.e. excluding all losses), we can infer that the generation rate for the broadband polarization-entangled triplet component is $6 \times 10^6 \text{ s}^{-1} \text{ mW}^{-1}$ over a bandwidth of 320 GHz. This is a significantly higher brightness than those for previously reported sources. The improvement in production efficiency is due to the use of a highly nonlinear crystal, KTP, and collinear propagation in a long crystal.

We should also point out that the singly resonant mode pairs can also be utilized if this narrowband component can be tuned to frequency degeneracy and frequency selected using a moderately narrowband filter cavity. Based on the generation rates R_0 and R_1 , and the number of singly resonant modes ($2B_{\text{PM}}/\text{FSR} \approx 115$), we can infer that a singly resonant mode pair would have a generation rate of $6 \times 10^4 \text{ s}^{-1} \text{ mW}^{-1}$ over a 30 MHz bandwidth, suggesting that this is a viable method for obtaining narrowband entangled photons.

In future experiments we would like our output wavelength to be near the Rb atom's 795 nm line where the quantum efficiency of a Si SPD reaches 50%. Also, alternative configurations such as a singly resonant cavity or a single-pass nonresonant arrangement will be attempted in the hope of obtaining stronger quantum interference.

Acknowledgments

This research was supported by US Army Research Office grant DAAD19-00-1-0177 and by National Reconnaissance Office contract NRO000-00-C0032.

References

- [1] Bennett C H, Brassard G, Crépeau C, Jozsa R, Peres A and Wootters W K 1993 *Phys. Rev. Lett.* **70** 1895–9
- [2] Ekert A K 1991 *Phys. Rev. Lett.* **67** 661–3
- [3] Kwiat P G, Mattle K, Weinfurter H, Zeilinger A, Sergienko A V and Shih Y 1995 *Phys. Rev. Lett.* **75** 4337–41
- [4] Kwiat P G, Waks E, White A G, Appelbaum I and Eberhard P H 1999 *Phys. Rev. A* **60** R773–6
- [5] Shapiro J H 2001 Long-distance high-fidelity teleportation using singlet states *Quantum Communication, Measurement, and Computing* 3 ed O Hirota and P Tombesi (New York: Kluwer) pp 367–74
- [6] Shapiro J H and Wong N C 2000 *J. Opt. B: Quantum Semiclass. Opt.* **2** L1–4
- [7] Lloyd S, Shahriar M S, Shapiro J H and Hemmer P R 2001 *Phys. Rev. Lett.* **87** 167903
- [8] Shapiro J H 2001 Architectures for long-distance quantum communication *Proc. 7th Int. Conf. on Squeezed States and Uncertainty Relations (Boston)*
- [9] Lee D and Wong N C 1993 *J. Opt. Soc. Am. B* **10** 1659–67
- [10] Lai B, Wong N C and Cheng L K 1995 *Opt. Lett.* **20** 1779–81
- [11] Teja J and Wong N C 1998 *Opt. Express* **2** 65–71
- [12] Shapiro J H and Sun K X 1994 *J. Opt. Soc. Am. B* **11** 1130–41